Low-coercive-field ferroelectric hafnia with mobile domain walls

Jing Wu,[1, *] Jiyuan Yang,[1, *] Yang Sun,[2] and Shi Liu[1, 3, †]

[1]*Key Laboratory for Quantum Materials of Zhejiang Province,*

Department of Physics, School of Science,

Westlake University, Hangzhou, Zhejiang 310024, China

[2]*Department of Physics, Xiamen University, Xiamen 361005, China*

[3]*Institute of Natural Sciences, Westlake Institute for Advanced Study,*

Hangzhou, Zhejiang 310024, China

Abstract

The high coercive field ($\mathcal{E}_c$) of hafnia-based ferroelectrics presents a major obstacle to their applications. The ferroelectric switching mechanisms in hafnia that dictate $\mathcal{E}_c$, especially those related to nucleation-and-growth at the domain wall (DW), have remained elusive. Through deep-learning-assisted multiscale simulations, we determine the finite-temperature thermodynamics and switching mechanisms for diverse types of 180° DWs, revealing a complex, stress-sensitive mobility landscape. The propagation velocities for mobile DW types under various thermal conditions can be characterized with a single creep equation, featuring a creep exponent of 2. This unconventional critical exponent results from the nucleation of a half-unit-cell-thin, elliptically-shaped critical nucleus. Our multiscale approach not only reproduces the experimental thickness (d) scaling, $\mathcal{E}_c \propto d^{-\frac{2}{3}}$, but also predicts that $\mathcal{E}_c$ of HfO_2 can be engineered to $\approx$0.1 MV/cm, even lower than perovskite ferroelectrics. The theoretical lower bound of $\mathcal{E}_c$ afforded by ferroelectric hafnia offers opportunities to realize power-efficient, high-fidelity ferroelectric nanoelectronics.

---

[*] These two authors contributed equally

[†] liushi@westlake.edu.cn

Ferroelectric hafnia is emerging as a viable candidate for incorporating ferroelectric capabilities into semiconductor technologies for its nanoscale ferroelectricity and proven compatibility with silicon [1, 2]. The $Pca2_1$ phase of HfO_2 is widely acknowledged as the ferroelectric phase in thin films [3–6]. The discovery of switchable spontaneous polarization in this fluorite-structured binary oxide has significantly advanced our understanding of ferroelectric physics, an area historically focused on perovskite oxides. For example, recent investigations have uncovered several unique aspects of hafnia-based ferroelectrics, including its metastable nature compared to the bulk monoclinic phase [5], the presence of flat phonon bands [7], and intertwined polar-nonpolar structural polymorphism with oxygen vacancy diffusion [8, 9].

However, the widespread applications of ferroelectric hafnia-based devices are mainly hindered by reliability issues, especially their limited endurance [10]. Unlike devices based on perovskite ferroelectrics like $Pb(Zr,Ti)O_3$ and $BiFeO_3$, which can be made close to fatigue-free [11], hafnia-based devices, depending on their architectures, typically exhibit poor endurance, with switching cycles ranging between 10^5 and 10^{12} [12–15]. This falls short of the required $> 10^{15}$ cycles for embedded random access memory. Such a detrimental issue is attributed to the high coercive field ($\mathcal{E}_c$, the electric field needed to switch the polarization) of hafnia-based ferroelectrics (typically >1 MV/cm in polycrystalline thin films and >2 MV/cm in epitaxial thin films) [16–18]. Repeated applications of high electric fields near the breakdown strength to reverse the polarization are expected to accelerate breakdown, causing rapid performance deterioration. Reducing $\mathcal{E}_c$ without sacrificing nanoscale ferroelectricity of hafnia has become a pressing challenge for the development of fast, durable, and energy-efficient nanoelectronics.

The atomic-level switching mechanisms affecting $\mathcal{E}_c$ in ferroelectric hafnia remain elusive, due to the multiple competing pathways and the complex variety of domain walls (DWs), which are interfaces separating differently polarized domains. Previous studies using zero-Kelvin density functional theory (DFT) have focused on polarization switching at the unit-cell level [3, 19] and the behavior of specific types of DWs [7, 20–22]. These studies overlooked the thermally activated nucleation-and-growth process, a crucial aspect for accurate $\mathcal{E}_c$ predictions [23]. Here, utilizing a deep neural network-based force field trained exclusively on first-principles data of hafnia [24, 25], we employ large-scale molecular dynamics (MD) simulations to investigate the finite-temperature thermodynamics and kinetics of all types of 180° DWs, identified through comprehensive symmetry analysis. Computational

details are provided in Supplementary Sect. I and an online notebook [26] is developed to share details regarding the machine-learning force field.

Our MD simulations unveil, without *a priori* assumptions, a stress-tunable, spontaneous transformation of DW type at room temperatures, which plays a critical role in the "divide-and-conquer"-like mechanism underpins the low switching fields for two types of DWs. We quantify the temperature- and field-dependence of propagation velocities for these walls in HfO_2, revealing a universal creep exponent of $\mu = 2$ and the underlying nucleation-and-growth mechanisms characterized by a half-unit-cell-thin, elliptically-shaped critical nucleus. A Landau–Ginzburg–Devonshire (LGD) analytical model incorporating this insight is developed, reproducing the experimentally observed thickness (d) scaling of $\mathcal{E}_c$ in thin films, $\mathcal{E}_c \propto d^{-2/3}$. Importantly, we demonstrate that the intrinsic $\mathcal{E}_c$ of HfO_2 determined by mobile DWs is, unexpectedly, on par with $Pb(Ti,Zr)O_3$, and can be as low as 0.1 MV/cm in thin films.

Classification of 180° DWs based on symmetry

We start with a symmetry analysis to classify all possible 180° DWs, interfaces separating domains with opposite polarization. The unit cell of $Pca2_1$ HfO_2 has a nonpolar layer of fourfold-coordinated oxygen ions (O^{np}) and a polar layer of threefold-coordinated oxygen ions (O^p), and these layers are ordered alternately (Fig. 1**a**). Application of Euclidean transformations within the unit cell results in eight different representations (Fig. S7). This feature, refereed to as conditional chirality [27], leads to a rich spectrum of 180° DWs. We introduce a mode vector $(T_x^\alpha, A_z^\beta, P_z^\gamma)$ with (α, β, $\gamma = \pm 1$) denoting the sign of the mode amplitude, to label the unit-cell configuration, where the tetragonal mode (T_x^α), the antipolar mode (A_z^β), and the polar mode (P_z^γ) are the three main modes bridging the cubic phase and polar orthorhombic phase with polarization aligned along the z axis (P_z) [28]. The T_x and A_z mode are characterized by antiparallel x-displacements and z-displacements of neighboring oxygen ions (Fig. 1**a**), respectively.

A general 180° wall can be expressed as $[T_x^\alpha A_z^\beta P_z^- | T_x^{\alpha'} A_z^{\beta'} P_z^+]$, allowing for 16 configurations (Fig. S8). As illustrated in Fig. 1**b**, these configurations can be further classified based on the sign of $\alpha \cdot \alpha'$ and $\beta \cdot \beta'$. In cases where $\text{sgn}(\alpha \cdot \alpha') > 0$, the x-displacement pattern of oxygen atoms across the DW remains unchanged, whereas $\text{sgn}(\alpha \cdot \alpha') < 0$ indicates a sign reversal of the T_x mode. For $\text{sgn}(\beta \cdot \beta') > 0$, the oxygen atoms at the wall are of the same

type (either O^p or O^{np}), while a negative sign indicates O^p and O^{np} atoms are adjacent. Symmetry analysis reveals six unique 180° DWs, which are labeled as $[01|\bar{1}0]$, $[10|01]$, and $[10|\bar{1}0]$, along with their counterparts having the sign of the T_x mode reversed across the wall, denoted as $[01|\bar{1}0]^*$, $[10|01]^*$, and $[10|\bar{1}0]^*$. Here, "1"("$\bar{1}$") labels the O^p atom displaced along $+z$ ($-z$), and "0" represents the O^{np} atom (Fig. 1**c**). For clarity in the following discussion, $[01|\bar{1}0]$, $[10|01]$, and $[10|\bar{1}0]$ walls are also named as type-P, type-NP, and type-PNP, based on the type of oxygen atoms at the wall; their counterparts with reversed T_x mode are type-P*, type-NP*, and type-PNP*.

As shown in Fig. 1**d**, our DFT calculations of DW energy (σ_{DW}) reveal that the type-PNP* wall, resembling the antiferroelectric-like $Pbca$ phase, possesses the lowest energy ($\sigma_{\mathrm{PNP^*}}$), followed by type-P, type-NP, and type-PNP walls at 0 GPa. In contrast, the other two T_x-sign-reversed DWs, type-P* and type-NP*, are highly unstable. Interestingly, applying a compressive hydrostatic pressure of 2.5 GPa substantially destabilizes type-P compared to type-NP and type-PNP walls. It is noted that $\sigma_{\mathrm{PNP^*}} < 0$ is an expected consequence of $Pbca$ HfO$_2$ being lower in energy than $Pca2_1$ HfO$_2$. Previously, this intriguing negative DW energy led to the proposal that each polar layer in $Pca2_1$ HfO$_2$ is strongly localized, allowing for individual switching and scale-free ferroelectricity [7]. Many subsequent studies focused on the motion of a type-PNP* wall [20, 22], despite its substantial energy barrier of 1.3 eV [21]. We will demonstrate with MD simulations that the polarization switching in HfO$_2$ does not involve the type-PNP* wall as it is immobile.

Spontaneous transformation of DW types at room temperatures

An important discovery from our MD simulations, contrasting with earlier findings from DFT modeling, is the spontaneous change in DW type at room temperatures. At 300 K and 0 GPa, the type-NP wall is unstable, automatically transforming into the type-P wall through $O^{np} \rightarrow O^p$ (**0** $\rightarrow$ **1**). This change can be intuitively expressed as $[10|\mathbf{0}\bar{1}0\bar{1}] \rightarrow [10\mathbf{1}|\bar{1}0\bar{1}]$, where the wall shifts laterally by half a lattice constant along the y-axis, $b/2$. At a higher pressure of 2.5 GPa, a reverse transition of type-P→type-NP occurs spontaneously via $\bar{\mathbf{1}} \rightarrow \mathbf{0}$, and can be represented as $[01|\bar{\mathbf{1}}0\bar{1}0] \rightarrow [010|0\bar{1}0]$. The high-energy type-PNP wall remains stable at 300 K under both stress conditions. As we will elaborate below, this thermally-induced spontaneous transition between O^{np} and O^p atoms at the interface is pivotal for the dynamics of type-P and type-NP walls.

We then gauge DW mobility at 300 K by determining the lowest electric field strength ($\mathcal{E}_s$) that triggers DW propagation within 1 nanosecond in MD simulations, with results summarized in Fig. 1e. Our simulations reveal that the type-PNP* wall is essentially immobile, showing no movement under a substantial $\mathcal{E}$ of 7 MV/cm. Rather, the adjacent $-P_z$ domain undergoes polarization reversal, since this field strength is sufficient to drive single-domain (SD) switching within 1 nanosecond. This aligns with the high DFT-calculated energy barrier of 1.3 eV for moving a type-PNP* wall, compared to a considerably lower barrier of 0.22 eV for homogeneous SD switching [19]. The resistance of a type-PNP* wall to $\mathcal{E}$ stems from the inability of a z-axis field to flip T_x mode that features antipolar x-displacements of oxygen atoms. For T_x-sign-conserved DWs, a wall with a lower σ_{DW} value mobilize more readily under $\mathcal{E}$, similar to the trend observed in perovskite ferroelectrics [23]. Notably, the type-P wall at 0 GPa exhibits a minimal $\mathcal{E}_s$ of 0.36 MV/cm. At 2.5 GPa, the type-NP wall has the lowest $\mathcal{E}_s$ of 0.53 MV/cm. Our following discussions will focus on the most mobile type-P and type-NP walls.

Mechanisms and kinetics of domain wall motions from MD simulations

Figure 2a and c compare the SD switching to DW motion mechanisms extracted from finite-field MD simulations at 300 K. At 0 GPa, a type-P wall initially transforms into a type-NP wall that serves as a bridging state. Conversely, at 2.5 GPa, a type-NP wall progresses via a transient type-P wall. A common feature is the lateral one-unit-cell translation being accomplished through two half-unit-cell hops ($b/2$), with the initial hop kinetically determinant. This is markedly different from perovskite ferroelectrics, where DWs advance by one unit cell at a time [23, 29]. Such a "first-hop-limiting" mechanism naturally results from the thermally-induced spontaneous change in DW types. Specifically, as shown in Fig. 2c, under a downward $\mathcal{E}$, a type-P wall transitions through $\bar{1} \to 0$ to a type-NP wall. This type is thermodynamically unstable at 0.0 GPa, causing a spontaneous hop of $0 \to 1$. At 2.5 GPa, the type-NP wall moves $b/2$ via $0 \to 1$, forming an unstable type-P wall that then shifts another $b/2$ via $\bar{1} \to 0$. These findings also imply that the rate-limiting step can be manipulated by mechanical boundary conditions, being either $\bar{1} \to 0$ at 0 GPa or $0 \to 1$ under higher pressure.

The unusual mechanisms of DW motions in HfO$_2$ revealed by MD are corroborated by DFT-based nudged elastic band (NEB) calculations. As plotted in Fig. 2d, the minimum

energy pathways (MEPs) at both pressures display clear two-hop characteristics: a larger barrier followed by a shallower one. The MEP for SD switching (Fig. 2**b**) also involves successive $0 \to 1$ and $\bar{1} \to 0$ hops, but the first hop is associated with a larger barrier. We propose that the presence of DWs decouples the movements of O^p and O^{np} atoms, rendering only one hop kinetically significant. This "divide-and-conquer"-like mechanism explains the lower switching fields for type-P and type-NP walls.

The velocities (v) for type-P and type-NP walls at 0 and 2.5 GPa, respectively, are quantified using MD simulations across various temperatures (T) and field strengths. For both stress conditions, as shown in Fig. 2**e-f**, the $\mathcal{E}$-dependence of v follows a creep process [30, 31]:

$$ v = v_0 \exp\left[-\frac{\mathcal{U}}{k_B T} \left(\frac{\mathcal{E}_{C0}}{\mathcal{E}} \right)^{\mu} \right], \tag{1} $$

where v_0 is the DW velocity under an infinite field, k_B is Boltzmann's constant, and $\mathcal{U}$ and $\mathcal{E}_{C0}$ represent the characteristic energy barrier and electric field at zero Kelvin, respectively; μ is the creep exponent, which depends on the dimensionality of the interface and the universality class of the disorder landscape pinning the interface [32]. Equation (1) can be reformulated as:

$$ v = v_0 \exp\left[-\left(\frac{\mathcal{E}_a}{\mathcal{E}} \right)^{\mu} \right], \tag{2} $$

where $\mu = 1$ corresponds to the famous Merz's law [33, 34], and $\mathcal{E}_a$ is the T-dependent activation field. By comparing Equations (1) and (2), $\mathcal{E}_a$ is given as $\mathcal{E}_a = (T_{C0}/T)^{1/\mu}$ with $T_{C0} = (\mathcal{U}/k_B)\mathcal{E}_{C0}^{\mu}$. Remarkably, all velocity data fits well with $\mu = 2$. This is evidenced by the linear relationship between $\ln v$ and $1/\mathcal{E}^2$ and an accurate representation of $\mathcal{E}_a$'s T-dependence as $\mathcal{E}_a = \sqrt{T_{C0}/T}$ (Fig. 2**g** and insets). A creep exponent of 2 is higher than the well-known value of $\mu = 0.25$ for 1D magnetic domain walls in ultrathin magnetic films [32] and $\mu = 1$ for 2D ferroelectric domain walls in typical perovskite ferroelectrics [23, 29].

Nucleation-and-growth at domain walls

We now develop an analytical model based on classical nucleation theory and Landau–Ginzburg–Devonshire (LGD) theory to explain the origin of $\mu = 2$ for both types of DWs. The DW motion can be understood as the formation of a quasi-two-dimensional nucleus with polarization aligned with $\mathcal{E}$ at the wall, followed by the growth of the nucleus. The energy of the critical nucleus gives the nucleation barrier (ΔU_{nuc}^*) which can be further related to $\mathcal{E}_a$ in equation (2) via the Avrami theory of transformation kinetics. We use a re-

6

vised persistent-embryo method (rPEM) [35] based on MD simulations to determine the size (N^*) and shape of the critical nucleus at the DW (see Supplementary Sect. I). Specifically, a two-dimensional (2D) embryo with N_0 switched oxygen atoms is initially embedded in the unswitched DW, and a tunable harmonic potential is applied to each oxygen atoms in the embryo to prevent back-switching. The potential is gradually weakened and completely removed when the nucleus size (N) surpasses a subcritical threshold (N_{sc} and $N_0 < N_{sc} < N^*$). The plateau of the $N(t)$ curve then corresponds to the period over which the nucleus size fluctuates around N^*.

Figure 3a displays the $N(t)$ curve for the type-P wall at 0.0 GPa, 300 K, and $\mathcal{E} = 0.45$ MV/cm, revealing multiple plateaus, from which the average of N^* is determined to be 38. The rate-limiting step of $\bar{1} \to 0$ involves a half-unit-cell-thin critical nucleus in the xz plane consisting of O^{np} atoms. This nucleus is elliptical, measuring $l_x^* = 1.7$ nm in width and $l_z^* = 2.7$ nm in height (Fig. 3c). For the type-NP wall at 2.5 GPa and 300 K under $\mathcal{E} = 0.55$ MV/cm, the $N(t)$ curve in Fig. 3b yields a half-unit-cell-thin, elliptically-shaped critical nucleus of O^p atoms, and the dimensions are $l_x^* = 3.2$ nm and $l_z^* = 5.9$ nm.

Having determined the shape of the critical nucleus, we can now proceed to develop a LGD nucleation model. For an elliptical nucleus of size $l_x \times l_y \times l_z$, its boundary within the xz plane is conveniently described with polar coordinates l_θ and θ. Here, l_θ is given by $l_\theta = l_x l_z / \sqrt{(l_x \sin\theta)^2 + (l_z \cos\theta)^2}$. In terms of the local displacement of oxygen atom (p_z) along the polar axis, the atomistic profile for a type-P or type-NP wall containing a nucleus can be represented by a single generalized equation:

$$p_z^{\text{nuc}}(y, \rho, \theta) = p_s \left[f(y, l_y, \delta_y) f(\rho, l_\theta, \delta_\theta) + g(y, l_y, \delta_y) \right], \tag{3}$$

where $f(q, l, \delta) = \frac{1}{2} \left[\tanh\left(\frac{q+l/2}{\delta/2} \right) - \tanh\left(\frac{q-l/2}{\delta/2} \right) \right]$ and δ is the diffuseness parameter; $g(y, l_y, \delta_y) = -\frac{1}{2} \left[\tanh\left(\frac{y+l_y/2}{\delta_y/2} \right) + \lambda(-1)^n \right]$ with n being an integer derived from $\lfloor \frac{y+l_y/2}{b/2} \rfloor$ and λ taking 1 for a nucleus of O^{np} atoms and -1 for a nucleus of O^p atoms; p_s is the ground-state value for the local displacement of O^p. The p_z profiles in the yz and xz planes generated by equation (3) are shown in Fig. 3e and 3f for type-P and type-NP walls, respectively. In the presence of $\mathcal{E}$, the energy of a wall with a nucleus relative to the wall without any nucleus can be expressed as:

$$\Delta U_{\text{nuc}} = \Delta U_{\text{V}} + \Delta U_{\text{I}}, \tag{4}$$

with

$$\Delta U_{\mathrm{V}} = -\mathcal{E}\eta \int_{-\infty}^{\infty} \mathrm{d}y \int_{0}^{2\pi} \mathrm{d}\theta \int_{0}^{\infty} \rho \mathrm{d}\rho \left[p_z^{\mathrm{nuc}}(y,\rho,\theta) - p_z^{\mathrm{DW}}(y,\rho,\theta) \right], \tag{5}$$

and

$$\Delta U_{\mathrm{I}} = \int_{-\infty}^{\infty} \mathrm{d}y \int_{0}^{2\pi} \mathrm{d}\theta \int_{0}^{\infty} \rho \mathrm{d}\rho \left\{ [U_{\mathrm{loc}}(p_z^{\mathrm{nuc}}) + U_x(p_z^{\mathrm{nuc}}) + U_y(p_z^{\mathrm{nuc}}) + U_z(p_z^{\mathrm{nuc}})] - \right.$$
$$\left. [U_{\mathrm{loc}}(p_z^{\mathrm{DW}}) + U_y(p_z^{\mathrm{DW}})] \right\}. \tag{6}$$

Here, ΔU_{V} is the electric field-polarization coupling term and ΔU_{I} is the energy penalty for creating new interfaces due to nucleation; η is a scaling constant that relates oxygen displacement p_z to local polarization; $p_z^{\mathrm{DW}} = p_s g(y, l_y, \delta_y)$ is the atomistic profile for a nucleus-free wall. Taking advantage of the 2D nature of the nucleus ($l_y = b/2$, $\delta_y = 0$) revealed from MD simulations, we can derive (see details in Supplementary Sect. IV) that $\Delta U_{\mathrm{V}} = -\frac{b}{16}\mathcal{E}\eta p_s \int_0^{2\pi} l_\theta^2 d\theta$, and ΔU_{I} is given as:

$$\Delta U_{\mathrm{I}} = \Delta U_{\mathrm{i}}' + \Delta U_{\mathrm{i}}$$
$$= \frac{b}{16} \int_0^{2\pi} \zeta'(l_\theta - \delta_\theta)^2 \mathrm{d}\theta + \left(\frac{b}{4} \int_0^{2\pi} \zeta l_\theta \delta_\theta \mathrm{d}\theta + \frac{b}{6} \int_0^{2\pi} \frac{l_\theta g_\theta p_s^2}{\delta_\theta} \mathrm{d}\theta \right) \tag{7}$$

We note that $\Delta U_{\mathrm{i}}'$ results from the change in DW type during the formation of a half-unit-cell-thin nucleus, where ζ' is proportional to the DW energy difference between type-P and type-NP walls, $|\sigma_{\mathrm{P}} - \sigma_{\mathrm{NP}}|$. This energy penalty is distinctive to DWs in HfO$_2$. In contrast, nucleation at DWs in perovskite ferroelectrics such as PbTiO$_3$ does not involve a change in the DW type that separates differently polarized domains (see Fig. S10). The term ΔU_{i} quantifies the energy penalty arising from polarization changes and their gradient at the nucleus boundary, where g_θ is the θ-dependent gradient coefficient along ρ, and ζ scales with the energy barrier of DW motion.

For a given $\mathcal{E}$, the energy of a 2D nucleus with the shape and size specified by l_θ depends on just a few parameters: p_s, η, ζ', ζ, and g_θ. All these parameters can be estimated straightforwardly with low costs. This enables the facile determination of N^* and $\Delta U_{\mathrm{nuc}}^*$ across a range of field strengths. As demonstrated in Fig. 3**g** and 3**i**, for both wall types, the values of N^* predicted by the LGD model show remarkable agreement with the results obtained from MD-based rPEM, confirming the validity and accuracy of the nucleation model as universally applicable to both type-P and type-NP walls. Interestingly, we find that $\Delta U_{\mathrm{nuc}}^*$ scales with the $1/\mathcal{E}^2$ (Fig. 3**h** and **j**), indicating the nucleation rate $J \propto \exp(-\frac{\Delta U_{\mathrm{nuc}}^*}{k_B T})$

can be reformulated as:

$$J = J_0 \exp\left[-\left(\frac{\mathcal{E}_{a,n}}{\mathcal{E}}\right)^2\right], \tag{8}$$

where J_0 is a pre-exponential factor and $\mathcal{E}_{a,n}$ is the effective activation field for nucleation. This further corroborates the finding that the creep exponent is $\mu = 2$ in equation (2). A series of model calculations are performed using a nucleation model without $\Delta U_i'$ to assess the impact of this unique energy term on the field-dependence of ΔU_{nuc}^*. We observe that omitting $\Delta U_i'$ recovers a linear relationship between ΔU_{nuc}^* and $1/\mathcal{E}$. These results demonstrate $\Delta U_i'$ is the atomistic origin for $\mu = 2$.

Intrinsic coercive fields from multiscale simulations

Based on Avrami's theory of transformation kinetics, we derive the relationship between ΔU_{nuc}^* and $\mathcal{E}_a$ for DW motions with $\mu = 2$ as $\mathcal{E}_a = \sqrt{\frac{1}{D+1}\frac{\lambda \Delta U_{nuc}^*}{k_B T}}\mathcal{E}$, where D represents the dimensionality and λ is a scaling parameter mapping ΔU_{nuc}^*, associated with a half-unit-cell hop, to the effective barrier encountered by a DW moving one unit cell at a time (see Supplementary Sect. V). With $D = 2$ and $\lambda = 0.5$, we compute $\mathcal{E}_a$ values using the LGD model at various temperatures, and the analytical values for two types of DWs agree with MD results (Fig. 4**a**). Utilizing the LGD model's efficient $\mathcal{E}_a$ prediction capability, we can conveniently predict the values of $\mathcal{E}_c$ by simulating the polarization-electric (P-$\mathcal{E}$) hysteresis loops resulting from DW motions (see Supplementary Sect. VI). As depicted in Fig. 4**b**, the P-$\mathcal{E}$ loop for type-P walls in HfO$_2$ at 0 GPa yields $\mathcal{E}_c \approx 0.1$ MV/cm, even lower than that of ≈ 0.2 MV/cm due to 180° DWs in Pb(Zr,Ti)O$_3$ thin films [23].

The analysis above suggests that the intrinsic coercive fields of hafnia-based ferroelectrics could be quite low. Yet, why do they often exhibit much larger $\mathcal{E}_c$ values experimentally [16–18]? We propose that this is due to a "thermodynamic-kinetic" dilemma unique to 180° DWs in HfO$_2$. The most thermodynamically stable 180° DW is the *Pbca*-like type-PNP* wall, which is immobile; whereas the type-P wall is the most mobile at room temperatures but its higher thermodynamic energy makes its formation in thin films rare. Therefore, the magnitude of $\mathcal{E}_c$ in hafnia-based thin films is likely determined by the SD switching process, which can also be predicted by our LGD nucleation model.

We first consider a single-crystal, single-domain HfO$_2$ thin film with a thickness d and a (111) orientation that is commonly observed in experiments. Assuming that $\mathcal{E}_c$ is the

minimum electric field required to extend the critical nucleus length to d, we determine the intrinsic E_c values as a function of d, plotted as a blue line in Fig. 4**c**. Notably, the theoretical $\mathcal{E}_c$ is $\approx$4 MV/cm for $d = 5$ nm, an excellent agreement with experimental values for La-doped HfO_2 [18] and $Hf_{0.5}Zr_{0.5}O_2$ films [36, 37] in the thin thickness limit where they are predominantly composed of ferroelectric phases. Furthermore, we consider the decreasing volume fraction of the polar phase with increasing thickness in polycrystalline thin films, by introducing a thickness-dependent p_s into the nucleation model (see Supplementary Sect. VII). Despite this simple treatment, our analytical values (red line in Fig. 4**c**) not only reproduce experimental results across various film thickness, but also the scaling relationship, $E_c \propto d^{-\frac{2}{3}}$, in epitaxial polycrystalline thin films [18, 36, 37].

Conclusions

In conclusion, we have developed a multiscale approach to elucidate the pivotal role of DW dynamics in dictating the coercive fields of ferroelectric HfO_2. Our finite-field MD simulations indicate that the *Pbca*-like DW, though extensively studied, actually plays a rather limited role in ferroelectric switching, and we have identified two mobile DW types. A thermally-induced spontaneous transformation of DW types is responsible for the unusual "first-hop-limiting" mechanism in the movements of mobile walls at room temperatures. The formation of a half-unit-cell-thin elliptical nucleus is identified, which supports the unconventional creep exponent of $\mu = 2$. The LGD analytical model, incorporating atomistic insights of nucleation, not only reproduces the experimentally observed thickness scaling of coercive fields in hafnia-based thin films but also uncovers an unexpectedly low intrinsic coercive field for HfO_2 due to mobile walls, rivaling that of perovskite ferroelectrics. Our results offer a deeper understanding of the fundamental mechanisms governing ferroelectric switching in this promising material, highlighting the potential for achieving ultralow coercive fields in hafnia-based ferroelectrics through domain wall engineering.

Author Contributions S.L. conceived and led the project. J.W. developed the force field, performed MD simulations, and analyzed the MD data. J.Y. identified the critical nucleus using rPEM with assistance from Y.S., derived the LGD analytical model, and predicted the coercive fields. All authors contributed to the discussion and the manuscript preparation.

Competing Interests The authors declare no competing financial or non-financial interests.

[1] T. S. Böscke, J. Müller, D. Bräuhaus, U. Schröder, and U. Böttger, Ferroelectricity in hafnium oxide thin films, Appl. Phys. Lett. **99**, 102903 (2011).

[2] U. Schroeder, M. H. Park, T. Mikolajick, and C. S. Hwang, The fundamentals and applications of ferroelectric HfO_2, Nat. Rev. Mater. **7**, 653–669 (2022).

[3] T. D. Huan, V. Sharma, G. A. Rossetti, and R. Ramprasad, Pathways towards ferroelectricity in hafnia, Phys. Rev. B **90**, 064111 (2014).

[4] X. Sang, E. D. Grimley, T. Schenk, U. Schroeder, and J. M. LeBeau, On the structural origins of ferroelectricity in HfO_2 thin films, Appl. Phys. Lett. **106**, 162905 (2015).

[5] R. Materlik, C. Künneth, and A. Kersch, The origin of ferroelectricity in $Hf_{1-x}Zr_xO_2$: A computational investigation and a surface energy model, J. Appl. Phys. **117**, 134109 (2015).

[6] M. H. Park, Y. H. Lee, H. J. Kim, Y. J. Kim, T. Moon, K. D. Kim, J. Müller, A. Kersch, U. Schroeder, T. Mikolajick, and C. S. Hwang, Ferroelectricity and antiferroelectricity of doped thin HfO_2-based films, Adv. Mater. **27**, 1811 (2015).

[7] H.-J. Lee, M. Lee, K. Lee, J. Jo, H. Yang, Y. Kim, S. C. Chae, U. Waghmare, and J. H. Lee, Scale-free ferroelectricity induced by flat phonon bands in HfO_2, Science **369**, 1343 (2020).

[8] P. Nukala, M. Ahmadi, Y. Wei, S. de Graaf, E. Stylianidis, T. Chakrabortty, S. Matzen, H. W. Zandbergen, A. Björling, D. Mannix, D. Carbone, B. Kooi, and B. Noheda, Reversible oxygen migration and phase transitions in hafnia-based ferroelectric devices, Science **372**, 630 (2021).

[9] L.-Y. Ma and S. Liu, Structural polymorphism kinetics promoted by charged oxygen vacancies in HfO_2, Phys. Rev. Lett. **130**, 096801 (2023).

[10] J. P. B. Silva, R. Alcala, U. E. Avci, N. Barrett, L. Bégon-Lours, M. Borg, S. Byun, S.-C. Chang, S.-W. Cheong, D.-H. Choe, J. Coignus, V. Deshpande, A. Dimoulas, C. Dubourdieu, I. Fina, H. Funakubo, L. Grenouillet, A. Gruverman, J. Heo, M. Hoffmann, H. A. Hsain, F.-T. Huang, C. S. Hwang, J. Íñiguez, J. L. Jones, I. V. Karpov, A. Kersch, T. Kwon, S. Lancaster, M. Lederer, Y. Lee, P. D. Lomenzo, L. W. Martin, S. Martin, S. Migita, T. Mikolajick, B. Noheda, M. H. Park, K. M. Rabe, S. Salahuddin, F. Sánchez, K. Seidel, T. Shimizu, T. Shiraishi, S. Slesazeck, A. Toriumi, H. Uchida, B. Vilquin, X. Xu, K. H. Ye, and U. Schroeder, Roadmap on ferroelectric hafnia- and zirconia-based materials and devices, APL Mater. **11**, 089201 (2023).

[11] C. A.-P. de Araujo, J. Cuchiaro, L. McMillan, M. Scott, and J. Scott, Fatigue-free ferroelectric capacitors with platinum electrodes, Nature **374**, 627 (1995).

[12] J. Y. Park, K. Yang, D. H. Lee, S. H. Kim, Y. Lee, P. R. S. Reddy, J. L. Jones, and M. H. Park, A perspective on semiconductor devices based on fluorite-structured ferroelectrics from the materials–device integration perspective, J. Appl. Phys. **128**, 240904 (2020).

[13] M. Pešić, F. P. G. Fengler, L. Larcher, A. Padovani, T. Schenk, E. D. Grimley, X. Sang, J. M. LeBeau, S. Slesazeck, U. Schroeder, and T. Mikolajick, Physical mechanisms behind the field-cycling behavior of HfO_2-based ferroelectric capacitors, Adv. Funct. Mater. **26**, 4601 (2016).

[14] E. Yurchuk, J. Müller, J. Paul, T. Schlösser, D. Martin, R. Hoffmann, S. Müeller, S. Slesazeck, U. Schröeder, R. Boschke, R. van Bentum, and T. Mikolajick, Impact of scaling on the performance of HfO_2-based ferroelectric field effect transistors, IEEE Trans. Electron Devices **61**, 3699 (2014).

[15] F. Ambriz-Vargas, G. Kolhatkar, M. Broyer, A. Hadj-Youssef, R. Nouar, A. Sarkissian, R. Thomas, C. Gomez-Yáñez, M. A. Gauthier, and A. Ruediger, A complementary metal oxide semiconductor process-compatible ferroelectric tunnel junction, ACS Appl. Mater. Interfaces **9**, 13262 (2017).

[16] T. Mimura, T. Shimizu, H. Uchida, O. Sakata, and H. Funakubo, Thickness-dependent crystal structure and electric properties of epitaxial ferroelectric Y_2O_3-HfO_2 films, Appl. Phys. Lett. **113**, 102901 (2018).

[17] Y. Wei, P. Nukala, M. Salverda, S. Matzen, H. J. Zhao, J. Momand, A. S. Everhardt, G. Agnus, G. R. Blake, P. Lecoeur, B. J. Kooi, J. Íñiguez, B. Dkhil, and B. Noheda, A rhombohedral ferroelectric phase in epitaxially strained $Hf_{0.5}Zr_{0.5}O_2$ thin films, Nat. Mater. **17**, 1095–1100 (2018).

[18] T. Song, R. Bachelet, G. Saint-Girons, N. Dix, I. Fina, and F. Sánchez, Thickness effect on the ferroelectric properties of La-doped HfO_2 epitaxial films down to 4.5 nm, J. Mater. Chem. C **9**, 12224 (2021).

[19] L. Ma, J. Wu, T. Zhu, Y. Huang, Q. Lu, and S. Liu, Ultrahigh oxygen ion mobility in ferroelectric hafnia, Phys. Rev. Lett. **131**, 256801 (2023).

[20] W. Ding, Y. Zhang, L. Tao, Q. Yang, and Y. Zhou, The atomic-scale domain wall structure and motion in HfO_2-based ferroelectrics: A first-principle study, Acta Mater. **196**, 556 (2020).

[21] D.-H. Choe, S. Kim, T. Moon, S. Jo, H. Bae, S.-G. Nam, Y. S. Lee, and J. Heo, Unexpectedly low barrier of ferroelectric switching in HfO_2 via topological domain walls, Mater. Today **50**, 8 (2021).

[22] Y. Wu, Y. Zhang, J. Jiang, L. Jiang, M. Tang, Y. Zhou, M. Liao, Q. Yang, and E. Y. Tsymbal, Unconventional polarization-switching mechanism in (Hf, Zr)O_2 ferroelectrics and its implications, Phys. Rev. Lett. **131**, 226802 (2023).

[23] S. Liu, I. Grinberg, and A. M. Rappe, Intrinsic ferroelectric switching from first principles, Nature **534**, 360 (2016).

[24] L. Zhang, J. Han, H. Wang, R. Car, and W. E, Deep potential molecular dynamics: A scalable model with the accuracy of quantum mechanics, Phys. Rev. Lett. **120**, 143001 (2018).

[25] J. Wu, Y. Zhang, L. Zhang, and S. Liu, Deep learning of accurate force field of ferroelectric HfO_2, Phys. Rev. B **103**, 024108 (2021).

[26] Low-coercive-field ferroelectric hafnia with ultrafast domain walls, `https://nb.bohrium.dp.tech/user/update/52795761357`.

[27] G.-D. Zhao, X. Liu, W. Ren, X. Zhu, and S. Yu, Symmetry of ferroelectric switching and domain walls in hafnium dioxide, Phys. Rev. B **106**, 064104 (2022).

[28] S. Zhou, J. Zhang, and A. M. Rappe, Strain-induced antipolar phase in hafnia stabilizes robust thin-film ferroelectricity, Sci. Adv. **8**, eadd5953 (2022).

[29] Y. H. Shin, I. Grinberg, I. W. Chen, and A. M. Rappe, Nucleation and growth mechanism of ferroelectric domain-wall motion, Nature **449**, 881 (2007).

[30] T. Tybell, P. Paruch, T. Giamarchi, and J. Triscone, Domain wall creep in epitaxial ferroelectric $Pb(Zr_{0.2}Ti_{0.8})O_3$ thin films, Phys. Rev. Lett. **89**, 097601 (2002).

[31] J. Jo, S. Yang, T. Kim, H. Lee, J. Yoon, S. Park, Y. Jo, M. Jung, and T. W. Noh, Nonlinear dynamics of domain-wall propagation in epitaxial ferroelectric thin film, Phys. Rev. Lett. **102**, 045701 (2009).

[32] S. Lemerle, J. Ferré, C. Chappert, V. Mathet, T. Giamarchi, and P. Le Doussal, Domain wall creep in an ising ultrathin magnetic film, Phys. Rev. Lett. **80**, 849 (1998).

[33] W. J. Merz, Domain formation and domain wall motions in ferroelectric $BaTiO_3$ single crystals, Phys. Rev. **95**, 690 (1954).

[34] R. C. Miller and G. Weinreich, Mechanism for the sidewise motion of 180° domain walls in barium titanate, Phys. Rev. **117**, 1460 (1960).

[35] Y. Sun, H. Song, F. Zhang, L. Yang, Z. Ye, M. I. Mendelev, C.-Z. Wang, and K.-M. Ho, Overcoming the time limitation in molecular dynamics simulation of crystal nucleation: A persistent-embryo approach, Phys. Rev. Lett. **120**, 085703 (2018).

[36] T. Song, R. Bachelet, G. Saint-Girons, R. Solanas, I. Fina, and F. Sánchez, Epitaxial ferro-electric La-doped $Hf_{0.5}Zr_{0.5}O_2$ thin films, ACS Appl. Electron. Mater. **2**, 3221 (2020).

[37] J. Lyu, I. Fina, J. Fontcuberta, and F. Sanchez, Epitaxial integration on Si (001) of ferroelectric $Hf_{0.5}Zr_{0.5}O_2$ capacitors with high retention and endurance, ACS Appl. Mater. Interfaces **11**, 6224 (2019).
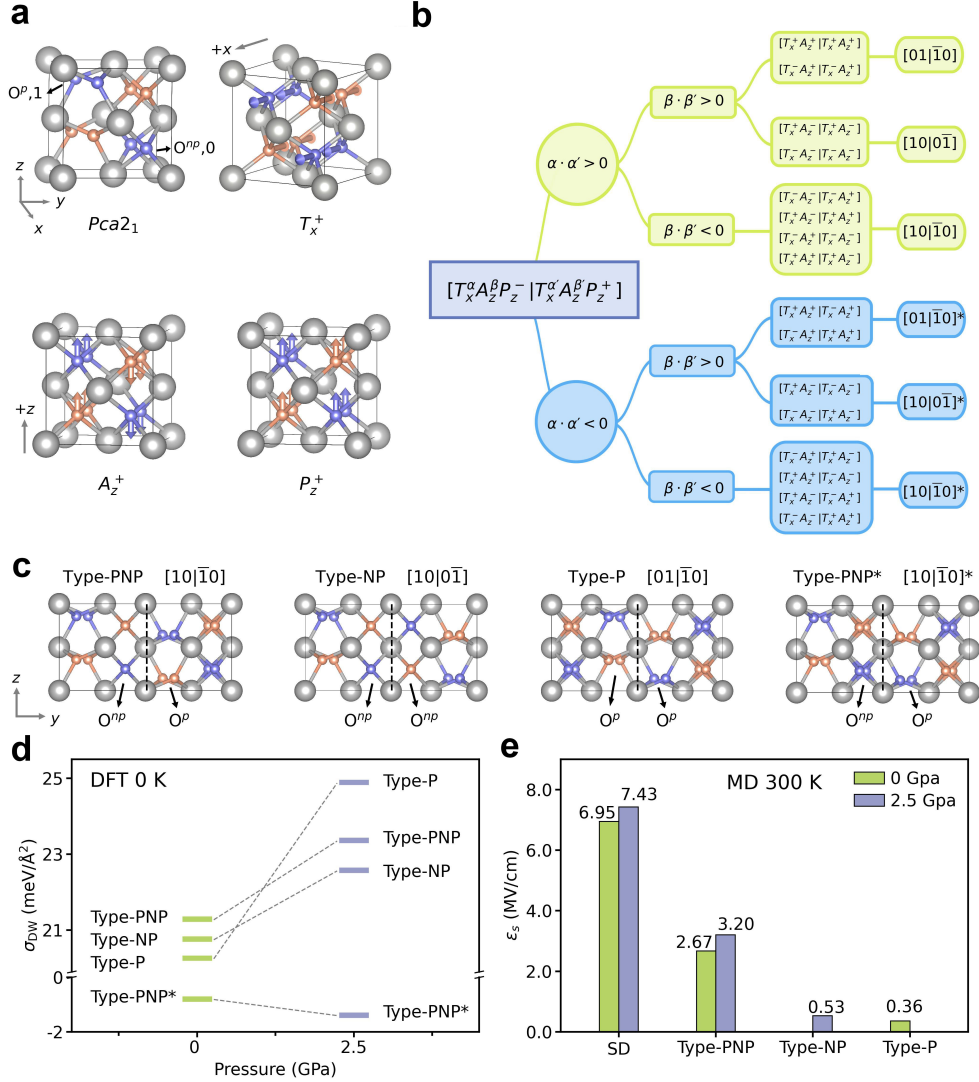
FIG. 1. **Classification of 180° domain walls in ferroelectric HfO$_2$. a,** Schematic representation of the unit cell of $Pca2_1$ HfO$_2$ and three modes, T_x^-, A_z^+, and P_z^+, in the cubic phase. According to the T_x^- mode, oxygen atoms with $+x$ and $-x$ displacements are colored in purple and salmon, respectively. **b,** Classification of a 180° wall represented as $[T_x^\alpha A_z^\beta P_z^- | T_x^{\alpha'} A_z^{\beta'} P_z^+]$. **c,** Illustrations of four different types of DWs, named based on the type of oxygen atoms (O^p and O^{np}) at the wall. The O^p atom displaced along $+z$ ($-z$) is labeled as "1" ("$\bar{1}$"), while the O^{np} atom is denoted as "0". **d,** Domain wall energies (σ_{DW}) under two different stress conditions determined by zero-Kelvin DFT calculations. **e,** Comparison of switching fields ($\mathcal{E}_s$) for a single domain (SD) and DWs at 0 and 2.5 GPa, as obtained with finite-field MD simulations at 300 K. The value of $\mathcal{E}_s$ is defined the minimum field strength required to initiate DW propagation within 1 nanosecond.
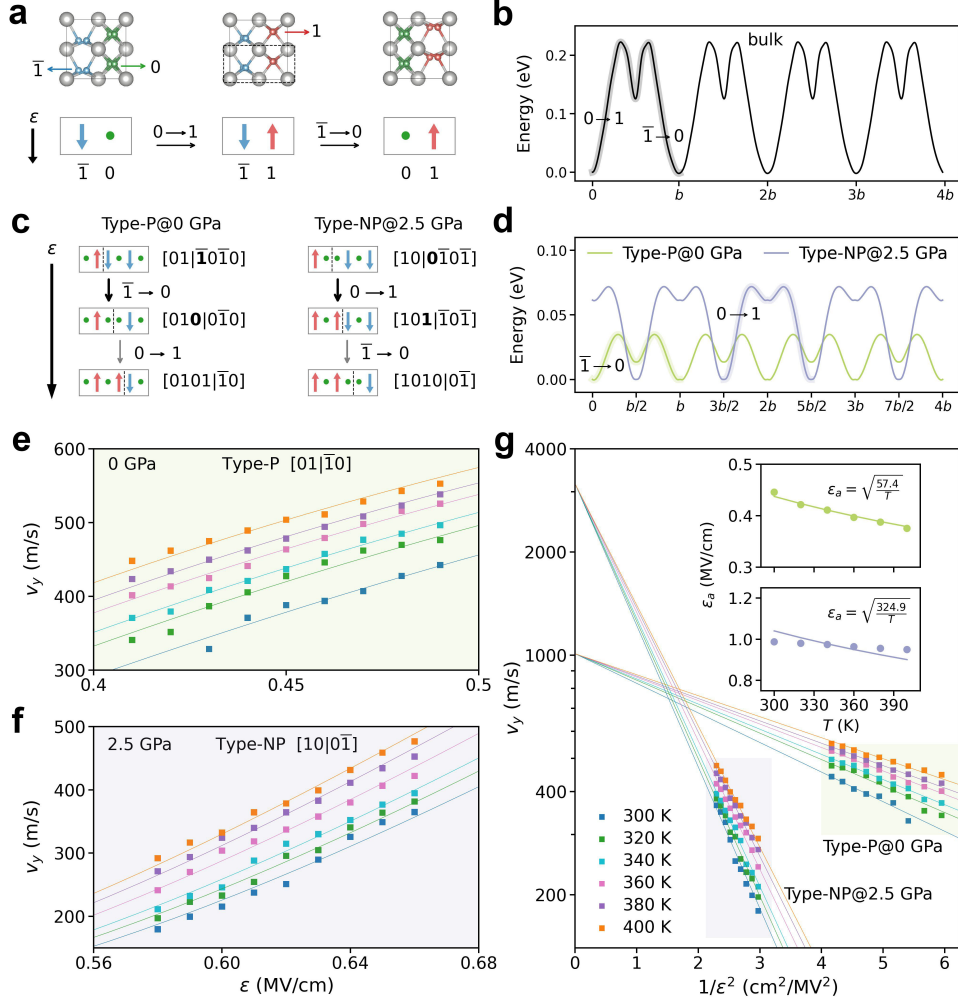
16

FIG. 2. **Kinematics of 180° domain walls in HfO$_2$. a,** Mechanism of polarization reversal in a unit cell. Oxygen atoms are color-coded based on the local displacements along the z axis, represented as arrows for O^p and green dots for O^{np} in the schematics. **b,** Energy profile for unit-cell-switching obtained with DFT-based NEB calculations. **c,** Mechanisms deduced from MD simulations for the motions of type-P walls at 0 GPa (left) and type-NP walls at 2.5 GPa (right). **d,** DFT energy profiles for DW motions. The rate limiting step is $\bar{1} \rightarrow 0$ for type-P walls at 0 GPa and $0 \rightarrow 1$ for type-NP walls at 2.5 GPa. Temperature (T)- and field ($\mathcal{E}$)-dependent DW velocity (v_y) for **e,** type-P walls and **f,** type-NP walls. Solid lines are fits with $v_y = v_0 \exp\left(-(\frac{\mathcal{E}_a}{\mathcal{E}})^\mu\right)$ and $\mu = 2$. **g,** Plots of $\ln(v_y)$ versus $1/\mathcal{E}^2$ for two wall types under varying temperatures. Insets show that the temperature dependence of the activation field can be well described by $\mathcal{E}_a = \sqrt{T_{C0}/T}$, supporting $\mu = 2$.
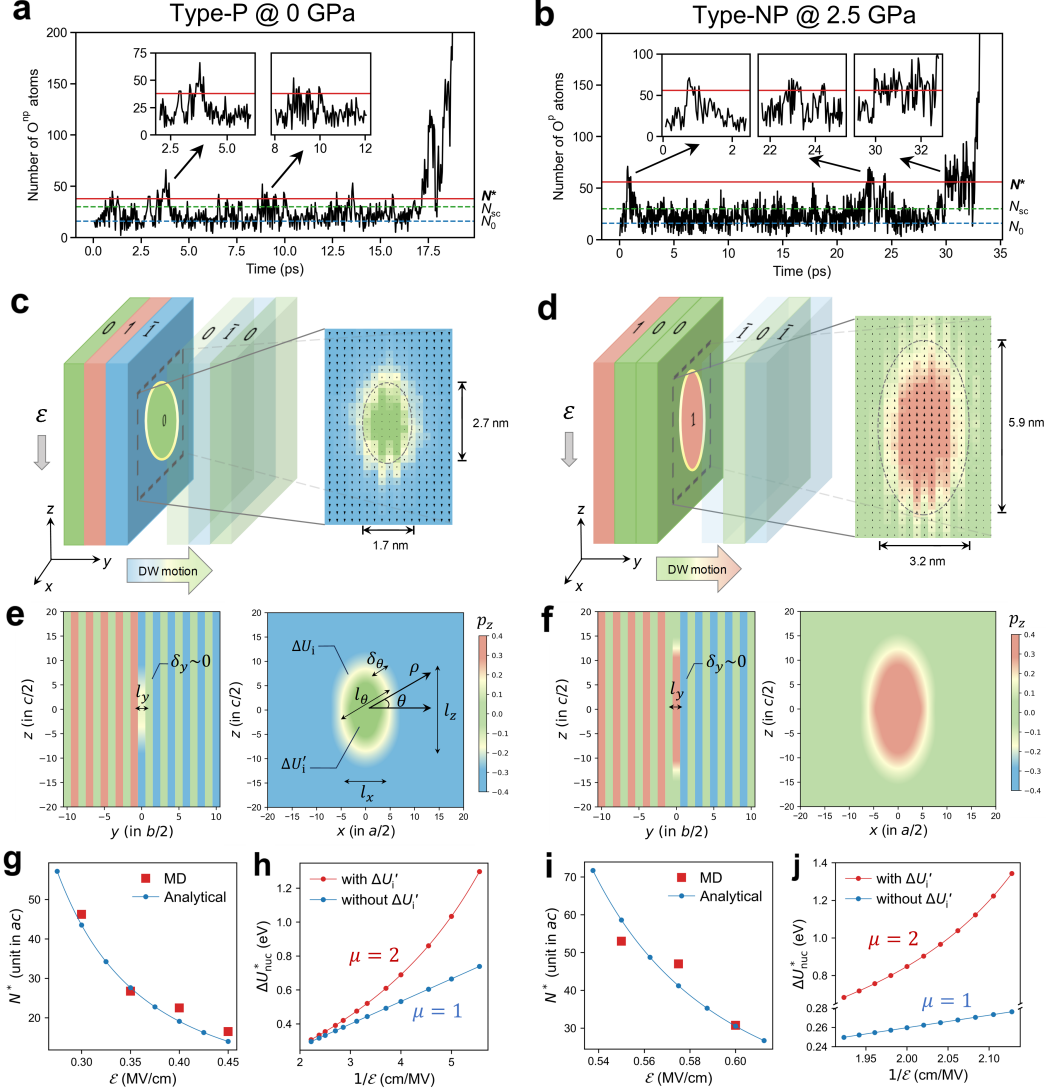
17

FIG. 3. **Nucleation and growth at domain walls.** Nucleus size (N) versus time during the nucleation process at a **a,** type-P wall at 0 GPa and **b,** type-NP wall at 2.5 GPa, both obtained using the MD-based rPEM method at 300 K. Blue and green dashed lines indicate the size of the persistent 2D embryo (N_0) and sub-critical nucleus (N_{sc}, at which the harmonic bias is removed), respectively. The critical size (N^*) is shown with a red solid line. Insets illustrate plateaus where N fluctuates around N^*. Simulated atomistic profiles of a quasi-2D half-unit-cell-thin nucleus at a **c,** type-P and **d,** type-NP wall. The corresponding analytical p_z profiles generated by equation (3) are depicted in **e** and **f**, respectively. Comparison of N^* values from MD simulations with those from a LGD-based analytical model across various electric fields are presented in **g** and **i** for two wall types. In both cases shown in **h** and **j**, $\Delta U_{\mathrm{i}}'$ is responsible for the quadratic dependence of critical nucleation barrier ($\Delta U_{\mathrm{nuc}}^*$) on $1/\mathcal{E}$, explaining the emergence of a creep exponent $\mu = 2$.
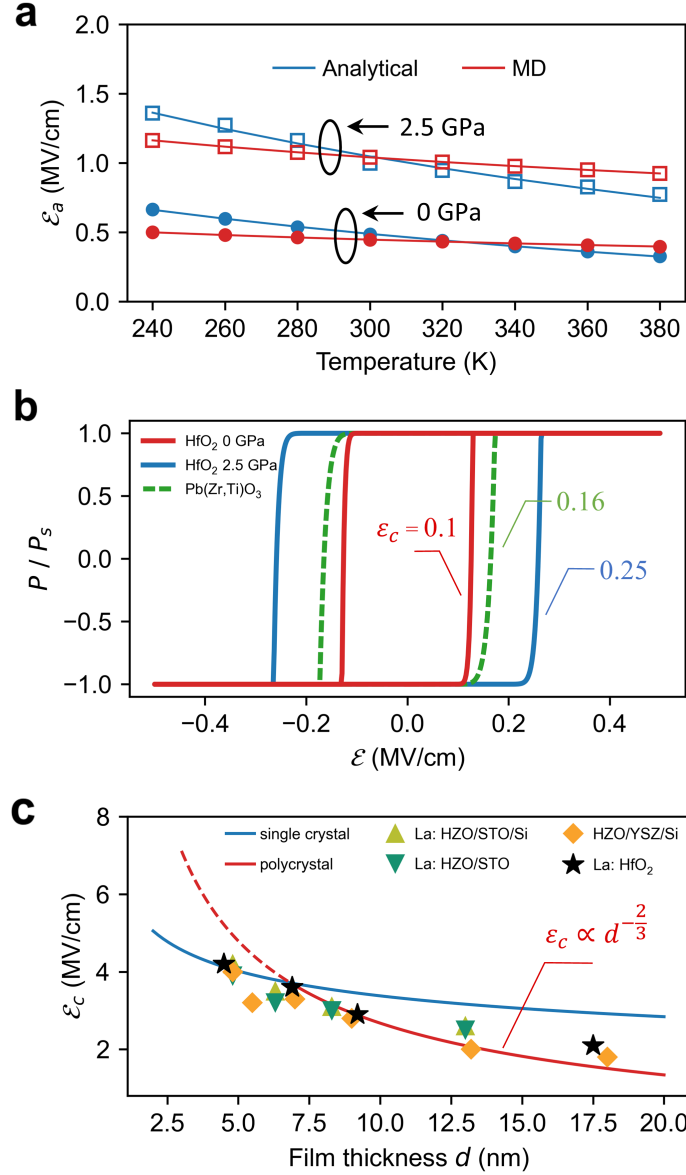
18

FIG. 4. **Coercive fields from multiscale simulations. a,** Comparison of the activation fields $\mathcal{E}_a$ in equation (2) for type-P and type-NP walls obtained from MD simulations with results estimated using the LGD analytical model. **b,** Intrinsic polarization-electric field hysteresis loops of HfO_2 thin films resulting from 180° DW motions. The simulated hysteresis loop for $Pb(Zr,Ti)O_3$ thin films is also plotted for comparison. **c,** Theoretical thickness-dependent coercive fields at the nucleation limit for both single-crystal and polycrystalline HfO_2 thin films, compared to experimental results for epitaxial thin films of La-doped HfO_2 [18] and $Hf_{0.5}Zr_{0.5}O_2$ (HZO) grown on common substrates such as $SrTiO_3$ (STO) [36] and yttria-stabilized zirconia (YSZ) [37].